Journal of Power Sources 189 (2009) 402–410

Contents lists available at ScienceDirect

Journal of Power Sources

journal homepage: www.elsevier.com/locate/jpowsour

On the electrochemistry of an anode stack for all-solid-state 3D-integrated batteries

L. Baggetto[a,*], J.F.M. Oudenhoven[a], T. van Dongen[b], J.H. Klootwijk[b], M. Mulder[b], R.A.H. Niessen[b], M.H.J.M. de Croon[a], P.H.L. Notten[a,b]

[a] Department of Chemical Engineering and Chemistry, Eindhoven University of Technology, Den Dolech 2, Postbus 513, 5600 MB Eindhoven, The Netherlands
[b] Philips Research Laboratories, High Tech Campus 4, 5656 AE Eindhoven, The Netherlands

ARTICLE INFO

Article history:
Received 18 July 2008
Accepted 24 July 2008
Available online 3 August 2008

Keywords:
All-solid-state batteries
3D-integration
Lithium ion
Lithium diffusion barrier layers
Silicon anode
Solid electrolyte interphase

ABSTRACT

This paper will report on the electrochemical and material characterization of a potential planar anode stack for all-solid-state 3D-integrated batteries. The first element of the stack is the silicon substrate. On top of silicon, a Li diffusion barrier layer material is deposited in order to effectively shield the substrate from the battery stack. Several materials are investigated with conventional electrochemical techniques. The best candidates, sputtered and atomic layer deposited (ALD) TiN, are studied in more detail with *ex situ* X-ray diffraction (XRD) and the reaction mechanism of these materials with Li is discussed. The third element of the stack is the active anode material. Thin films of poly-Si are studied towards their thermodynamic and kinetic properties. Moreover, the growth of SEI layers on top of poly-Si anodes cycled in two liquid electrolytes has been investigated by means of *ex situ* SEM. Strikingly, when poly-Si is covered with a solid-state electrolyte, prolonged lifetime is found, enabling future 3D-integrated all-solid-state batteries.

1. Introduction

In our modern society, miniaturized *autonomous devices* are expected to become increasingly important. Examples of such devices are small medical implants, hearing aids, integrated lighting solutions and many others. These devices induced a new electronic revolution, denoted as *ambient intelligence* [1]. This is generally considered as the next challenging development in the *knowledge age* [2,3]. In an effort to improve people's quality of life significantly, a higher level of miniaturization will be required for these devices in the near future.

Characteristic for small autonomous devices is that they have to operate wirelessly, implying that on-board electricity is essential. When devices are becoming smaller and smaller it becomes, however, much more complicated to assemble these from their individual components and the contribution of inactive overhead mass and volume by, for example, the package will increase significantly. As the energy consumption will be small for autonomous devices this opens up the possibility to integrate electricity storage devices, making autonomous devices highly efficient.

Electricity can be effectively stored in either capacitors or batteries. In comparison to integrated capacitors the amount of energy that can be stored in planar all-solid-state batteries is significantly higher [4,5]. Yet, it is often still not sufficient to power future autonomous devices. Therefore, it would be better to make use of 3D-structured substrates, which provide much larger effective surface areas and interesting possibilities towards integration. Various integration concepts have been proposed [6,7]. An overview has been given by Long et al. [6]. We adopt, however, a different approach, which aligns well with state-of-the-art IC technologies.

Fig. 1a presents a schematic representation of a 3D-integrated all-solid-state battery with a pore configuration [4,8,9]. This system is based on the intercalation of lithium ions as energy carrying particles and relies on the combination of various recent developments: (i) 3D etching of a silicon substrate in order to create high-aspect ratio structures; (ii) barrier layer technology, to effectively shield the silicon substrate from the battery stack and (iii) the use of novel high energy density electrode materials [4,8].

Defining, for example, the dimensions of the 3D-pore structure, by the horizontal pitch (H_p), the vertical pitch (V_p), the diameter (d) and height (h) (Fig. 1b), the surface area enlargement (A) can be calculated according to

$$A = 1 + \frac{\pi dh}{Ll}\left(\frac{L-(H_p-d)}{H_p}\right)\left(\frac{l-(V_p-d)}{V_p}\right) \quad (1)$$

* Corresponding author at: Department of Chemical Engineering and Chemistry, Eindhoven University of Technology, Den Dolech 2, Postbus 513, 5600 MB Eindhoven, The Netherlands. Tel.: +31 40 274 6247; fax: +31 40 274 3352.
E-mail address: l.baggetto@tue.nl (L. Baggetto).

0378-7753/$ – see front matter © 2008 Elsevier B.V. All rights reserved.
doi:10.1016/j.jpowsour.2008.07.076

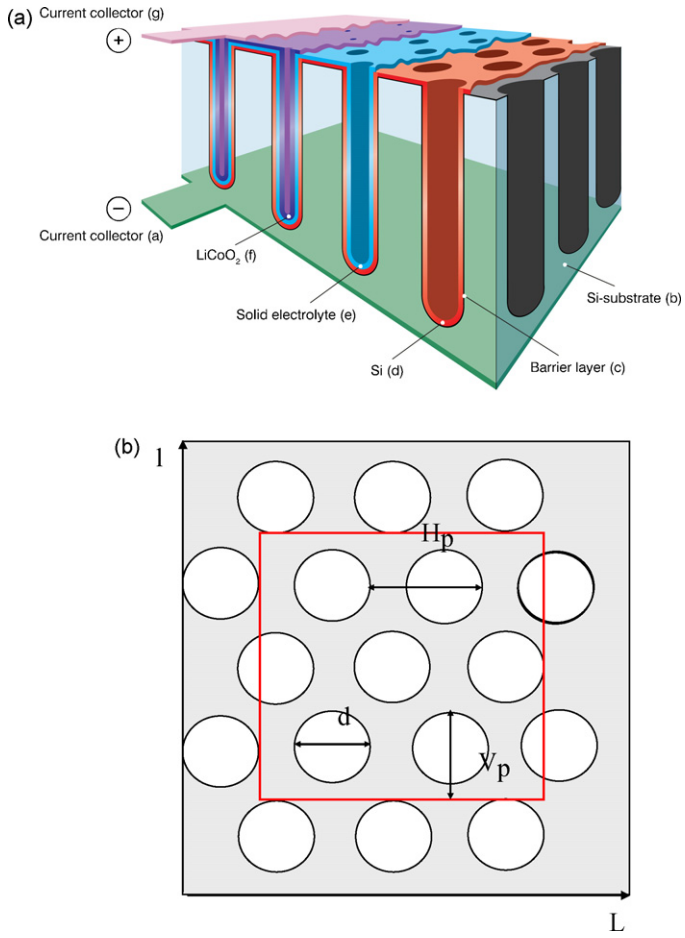

Fig. 1. (a) 3D-integrated all-solid-state battery to be applied as energy supply unit to power autonomous devices. The various layers, denoted from (a) to (g), are deposited in high-aspect ratio pores etched in, for example, silicon. (b) The geometry of the structure is characterized by footprint length (L), footprint width (l), pore diameter (d), and horizontal (H_p) and vertical (V_p) pitch.

where L and l represents the footprint length and width, respectively (Fig. 1b).

Using standard etching technology, an area enlargement of 25 can easily be achieved [10]. This surface area enlargement and the given energy density of the active materials will result in 3D-integrated batteries with storage capacity of approximately 1.5 mAh per micron of cathode material and cm^2 footprint area [4,8]. With an operating voltage of about 3.5 V ($LiCoO_2$ operates around 4 V and Si at about 0.5 V), a single-sided processed device is therefore expected to deliver about 5 mWh μm^{-1} cm^{-2} with an expected power capability in the range of 0.5–50 mW μm^{-1} cm^{-2}, using 0.1 and 10 C-rate currents, respectively, where 1 C-rate is defined as the current required to (dis)charge the battery in 1 h.

On the route towards 3D-integrated batteries, the electrochemistry of a potential anode stack is investigated. It comprises a substrate, a Li diffusion barrier layer and an anode material. First, results on several thin-film Li-barrier layer candidates will be presented. The aim of a Li diffusion barrier layer is twofold: it should be electronically conductive while being capable of efficiently blocking lithium species. To select potential Li barrier candidates (Ta, TaN and TiN), cyclic voltammetry (CV) and galvanostatic cycling were employed. The reaction mechanism for alloying nitrides is often related to a conversion reaction where the nitrogen in MN_x reacts irreversibly with Li to form Li_3N [11]. This conversion reaction is usually expressed as

$$MN_x + 3xLi \rightarrow M + xLi_3N \quad (2)$$

In the case of non-alloying elements M, the reaction presented in Eq. (2) is usually reversible [12]. As Ta and Ti do not alloy with Li [13,14], one could expect a reversible displacement reaction between TiN or TaN and Li. Our results will show that such reaction does not occur and that these materials are suitable Li barrier layers.

Moreover, the intercalation properties (thermodynamic and kinetic) of poly-Si anode thin-films were studied with Galvanostatic Intermittent Titration Technique (GITT) coupled with electrochemical impedance spectroscopy (EIS). The favorable influence of a solid-state electrolyte on the cycle-life performance of thin-film Si anodes was investigated together with transmission electron microscopy (TEM) and scanning electron microscopy (SEM). Our results will show the unfavorable impact of the solid electrolyte interphase (SEI) growth on the anode cycling performance and highlight the advantage of covering the silicon anode material with a solid-state electrolyte.

2. Experimental

2.1. Thin-film deposition

For the thin-film deposition process, (1 0 0) oriented 6 in. silicon substrates were used (n^{++}, resistivity of *ca.* 1–5 mΩ cm). Sputtered Ta, TaN and TiN diffusion barrier layers were deposited at room temperature by means of dc magnetron sputtering, using deposition conditions reported elsewhere [8]. Atomic layer deposition (ALD) TiN was grown using conditions reported elsewhere [15,16]. Low Pressure Chemical Vapor Deposition (LPCVD) poly-silicon films, 50 nm thick, were grown on top of Li diffusion barrier layers using conditions described in another publication [8]. LiPON RF-sputtering was performed using standard conditions reported in literature [4].

2.2. LPCVD poly-silicon thin-film patterning

In order to accurately control the surface area of the electrodes, the silicon thin films were further processed and patterned by means of standard lithography. The description of the preparation is reported elsewhere [8].

2.3. Thin-film characterization

The samples were prepared for TEM, using Focused Ion Beam (FIB200) equipment. TEM studies were performed using a TECNAI F30ST TEM operating at 300 kV. The samples were analyzed by SEM, using a Philips SEM XL40 FEG microscope with an incident electron beam of 10 kV. In order to determine the amount of active materials and their composition, Rutherford backscattering spectrometry (RBS) was employed in the so-called channeling condition [8]. Standard 2θ–ω X-ray diffraction (XRD) scans were recorded with a PANalytical X'Pert PRO MPD diffractometer, equipped with a Cu X-ray source. The analyzed area was about 5 mm × 5 mm, independent of the diffraction angle. To suppress the diffraction peaks of the single crystalline Si substrate, an ω-offset of 3° was applied. More information can be obtained if measurements are performed at different directions of the diffraction vector, which can be achieved by tilting the sample , yielding to pole diagrams. Such measurements were performed on the present samples using a Philips X'Pert PRO MRD diffractometer, equipped with a Cu X-ray source and a polycapillary X-ray lens in the incident beam (to

obtain an almost parallel X-ray beam). The beam size was set to about 4 mm × 4 mm; the analyzed area depends on the diffraction and sample tilt angles during the measurement. The peak intensity of the TiN 2 0 0 peak was recorded by setting the instrument at a fixed 2θ (about 42.5° for TiN 2 0 0) and tilting (0–90°) and rotating (0–360°) the sample during measurement.

2.4. Electrochemical investigation

Three-electrode cylindrical electrochemical cells, made of Teflon® and with a volume of about 40 ml, were assembled in an argon-filled glove-box. The diffusion barrier layers or the silicon electrodes were mounted as working electrodes while pure lithium foils were used as counter and reference electrodes. The liquid electrolytes, comprising of 1 M $LiClO_4$ dissolved in PC and 1 M $LiPF_6$ dissolved in EC/DEC, were provided by Puriel, Techno Semichem Co. Ltd., Korea. Detailed electrochemical experiments were conducted with the $LiClO_4$-based electrolyte. The cycle-life experiments were performed in both electrolytes. The cells were placed in a stainless steel holder that was thermostatically controlled at 25 °C. Contaminants in the glove-box (water and oxygen) were monitored and controlled below 1 ppm. Galvanostatic cycling was performed with a M4300 galvanostat (Maccor, Tulsa, USA). CV and GITT coupled with EIS were conducted with an Autolab PGSTAT30 (Ecochemie B.V., Utrecht, The Netherlands). GITT was programmed with about 40 incremental (dis)charge steps, separated by resting periods of 90 min. EIS was conducted at quasi-equilibrium after each GITT rest steps, using an AC voltage of 5 mV for a frequency range of 100 kHz to 10 mHz. The obtained impedance spectra were fitted with an Equivalent Circuit Tool.

3. Results and discussion

3.1. Lithium diffusion barrier layers

When lithium is intercalated in silicon, the volume expansion of the host material can be as high as 300%. This induces high compressive stress, which results in severe degradation of bulk silicon [8,17]. To prevent such irreversible damage and the loss of Li-ions from the active battery electrode, Li diffusion barrier materials are essential [8]. Various materials deposited by RF sputtering were investigated as potential diffusion barrier layer candidates. Fig. 2a shows the cyclovoltammograms of 70 nm thick Ta, TaN and TiN layers deposited on highly doped (n^{++}) planar Si substrates. Cyclovoltammetry is a powerful tool to measure the electrochemical fingerprint of electrochemical (in)active materials. The results clearly show that TiN (red curve) and TaN (blue curve) have a very low reactivity with respect to Li-ion intercalation, revealing low currents in the potential range of 0–3 V *vs.* Li/Li^+. On the other hand, pure Ta metal (green curve) shows substantial affinity towards lithium. This results in pronounced reduction and oxidation currents, which indicate a reversible and undesired insertion of lithium into and extraction of lithium from Ta, at around 0.2 and 0.4 V, respectively. The inset of Fig. 2a shows the constant-current charging and discharging results obtained with the same samples. These galvanostatic measurements provide useful information about the amount of charge involved during repeated cycling. As expected from the cyclovoltammograms, the storage capacities of the nitride-based materials are substantially lower than those of pure Ta films. From these results, it can be concluded that the use of nitrides as barrier layers is most beneficial, in particular TiN.

Fig. 2b depicts the charge density involved as a function of thickness of sputtered TiN thin films during galvanostatic (dis)charging

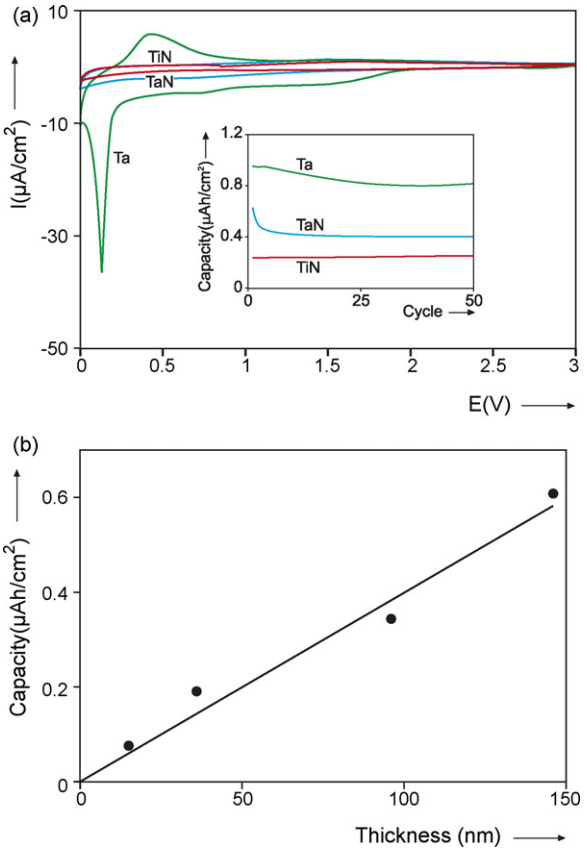

Fig. 2. (a) Reactivity of 70 nm thick sputtered Ta (green curve), TaN (blue curve) and TiN (red curve) diffusion barrier layers towards Li-ion. The main plot shows the cyclovoltammograms at 1 mV s^{-1} and the inset reveals the corresponding galvanostatic cycling capacities obtained at 3 μA cm^{-2} between 0 and 3 V *vs.* Li/Li^+. (b) Relationship between the charge density and the film thickness for sputtered TiN layers upon galvanostatic cycling at 3 μA cm^{-2} between 0 and 3 V *vs.* Li/Li^+.

experiments. The relationship between the capacity and thickness is linear and independent of the cycle number for more than 200 cycles. This linearity implies that the amount of charge, reversibly inserted in and extracted from TiN, is proportional to the amount of TiN and can therefore indeed be considered as a bulk effect. From the slope of this line the amount of Li involved can be calculated, which amounts to only 0.02 Li per TiN formula unit. For comparison, Ta reversibly inserts and extracts 0.09 Li per Ta atom. According to Eq. (2), the displacement reaction between TiN and Li would correspond to a transfer of 3 Li per TiN formula unit. As only 0.02 Li per TiN is transferred, it can be concluded that the displacement reaction does not occur. The corresponding reasons are not clear and might result from the fact that the reaction presents very poor kinetics or unfavorable thermodynamics. Nevertheless, these nitride materials present good barrier properties as no intercalation response into silicon is observed upon repeated cycling.

Even though the amount of 0.02 Li per TiN formula unit is extremely low, it is important to realize that traces of lithium, after diffusion from TiN, can disperse into the underlying bulk Si-substrate. It is known that metal contamination, such as copper but also lithium in dielectric films will strongly influence their electrical properties, which can, in turn, disrupt oxide-based integrated circuit devices [18]. Therefore, innovative solutions have to be found to further reduce this amount of Li possibly penetrating these TiN barrier layers.

Interesting possibilities might, for example, be offered by ALD, for which it is known that different structural properties can be

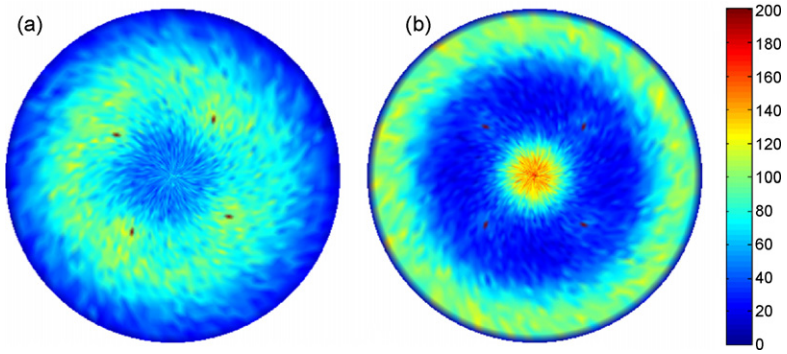

Fig. 3. Pole figures obtained from X-ray diffraction tilting experiments, showing the intensity of the TiN 2 0 0 peak as a function of tilt and rotation angles, of the sputtered (a) and ALD (b) TiN layers.

achieved [15,16,19]. Recently, Knoops et al. [15,16] reported the deposition and electrochemical characterization of TaN and TiN thin-films. It was found that ALD-grown TiN is more inert towards Li-ion (de)intercalation than sputtered TiN [15,16]. To understand this difference the samples were characterized with XRD. Tilting experiments were performed on the as-deposited material to check for preferred orientation. The results for the TiN 2 0 0 peak are plotted in Fig. 3. The centre of the pole figures corresponds to the untilted sample; the edge corresponds to 90° tilt (*i.e.* the side of the sample is measured). The intensities corresponding to the colours are given by the colour bar. If there is no preferred crystallographic orientation of the crystallites, the intensity in a pole figure should be more or less constant. In case of a preferred orientation, regions with high intensity will be visible in a pole figure.

The TiN 2 0 0 pole figure of the sputtered layer (Fig. 3a) shows a broad ring with somewhat higher intensity of the TiN 2 0 0 peak between tilt angles of about 45° and 65°. This corresponds to a slight preferred orientation of the TiN crystallites with their {1 1 1} lattice planes parallel to the sample surface (in cubic crystal structures the {2 0 0} lattice planes make an angle of 54.7° with the {1 1 1} lattice planes). There is no dependence of the intensity on the rotation angle. Hence, the layer has a slight fibre texture, with a <1 1 1> fibre axis parallel to the sample normal. The TiN 2 0 0 pole figure of the ALD layer (Fig. 3b) shows a higher intensity in the centre (0° tilt angle) and near the edge (90° tilt angle) of the figure. Thus, a preferred orientation of the TiN crystallites, with their {2 0 0} lattice planes parallel to the sample surface, is present for the ALD films. Moreover, there is no dependence of the intensity on the rotation angle, which means that the crystallites can take any orientation around the <1 0 0> direction perpendicular to the surface. Hence, the layer has a fibre texture, with a <1 0 0> fibre axis parallel to the sample normal. For both films, four intense spots are visible in the pole figures at a tilt angle of about 45° and originate from the Si substrate (the Si 2 2 0 peak is close to the TiN 2 0 0 peak). This difference in crystallites orientation between the ALD and sputtered TiN films probably explain the difference in reversible storage capacity [15,16].

Ex situ XRD was utilized to characterize possible changes in crystallographic structure before and after prolonged cycling. This characterization was performed on the ALD films. Fig. 4a shows the reversible storage capacity of a 70 nm thick ALD film for 250 cycles, which is lower than that of the sputtered material. The diffractograms of the as-deposited sputtered and ALD films and the diffractogram of the ALD film after cycling are presented in Fig. 4b. The broad peak around 69° originates from the Si substrate. As it was already observed from the tilting experiments, a strong 2 0 0 preferred orientation is visible for the ALD film and a slight 1 1 1 preferred orientation in the case of the sputtered layer. Moreover, the X-ray data do not reveal a noticeable difference between the as-deposited and cycled ALD TiN. As for sputtered TiN, ALD-grown TiN does not intercalate much Li (less than 0.02 Li per TiN formula unit). Therefore, these XRD results confirm that the reaction mechanism between TiN and Li does not occur via a displacement or conversion reaction. As the reversible storage capacity is proportional to the amount of material, surface reactions (SEI, native oxides. . .) cannot explain the origin of this reversible reaction.

The electrochemical and X-ray results confirm that TiN is a promising Li barrier candidate. ALD TiN is a particularly interesting material as it reacts even less than sputtered TiN [15,16]. Moreover, ALD is a suitable technique for growing step-conformal thin layers into 3D-structured substrates, enabling future 3D-integrated all-solid-state batteries.

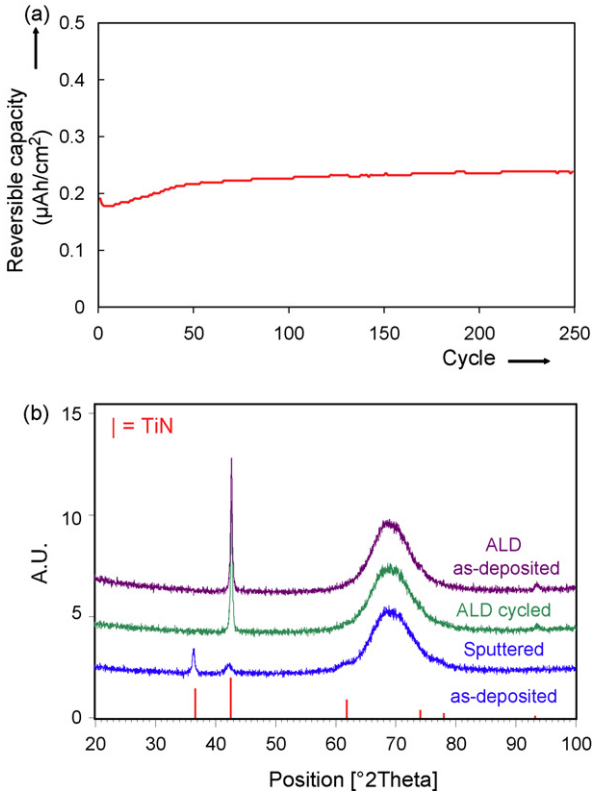

Fig. 4. (a) Reversible storage capacity of a 70 nm thick ALD-grown TiN film obtained upon galvanostatic cycling at 3 μA cm^{-2} between 0 and 3 V *vs.* Li/Li^+. (b) X-ray diffractograms of the as-deposited sputtered and ALD films and of the same ALD film after 250 galvanostatic cycles (a).

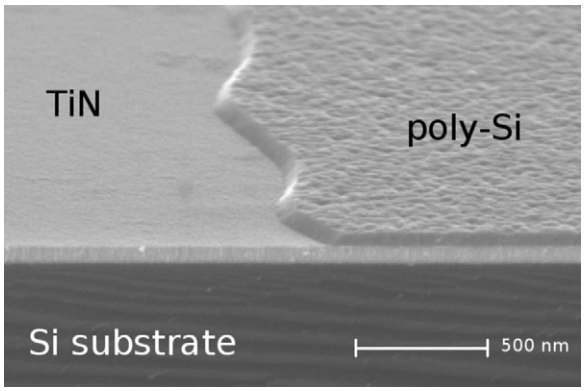

Fig. 5. SEM image of a freshly prepared anode stack made of n^{++} Si substrate/sputtered TiN/LPCVD poly-Si.

3.2. Investigation of LPCVD poly-Si thin-film electrochemistry: the anode/electrolyte interface

It was recently shown that LPCVD-grown poly-Si thin-film electrodes combine extremely high reversible electrochemical storage capacities with very high-rate capability and show a beneficial voltage profile and excellent lifetime characteristics when protected with a solid-state electrolyte [8]. The choice of utilizing silicon anodes lies in the fact that it shows the highest theoretical gravimetric and volumetric storage capacities towards lithium ion intercalation, *i.e.* 3579 mAh g^{-1} and 8303 mAh cm^{-3}, respectively, when assuming complete conversion into $Li_{15}Si_4$ [20]. Interestingly, Si is the parent material for the electronic industry and therefore highly attractive as processing material for battery integration [4].

Fig. 5 shows a SEM image of the TiN/poly-Si stack. A patterning procedure is performed on poly-Si in order to accurately control the amount of active anode material. Mass measurements were performed, using RBS. Knowing the precise mass is essential in obtaining accurate values for the storage capacity. Typically, a 50 nm Si layer with 1.8 cm^2 surface area is equivalent to an active mass of about 20 μg.

The thermodynamics of the poly-Si electrodes are determined as a function of the Li-content using GITT. The main plots of Fig. 6 present the equilibrium curves of poly-Si. The derivatives of the storage capacity with respect to the electrode potential are presented in the insets.

During the first intercalation of poly-Si (not presented here), the material transforms irreversibly into an amorphous structure [20]. The equilibrium curve, measured after this irreversible transformation, is divided into two parts: insertion (curve (a)) and extraction (curve (b)) of Li-ions. By starting from the Li-depleted state (0 Li per Si atom), charge transfer takes place at the silicon/electrolyte interface and Li subsequently alloys with Si. Two quasi-plateaus are clearly visible when the potential decreases down to 50 mV (Fig. 6a). These quasi-plateaus are representative of reversible amorphous phase transitions of silicon into lithiated silicon [8,20]. Upon further charging a small plateau is observed (Fig. 6b). This plateau is representative of the crystallization of amorphous lithiated Si into $Li_{15}Si_4$ [20]. Although $Li_{15}Si_4$ has not been reported in the Li–Si binary phase diagrams [21], it can apparently be formed electrochemically at room temperature. Extracting Li from a fully lithiated electrode (curve (b)) induces the single-step conversion of $Li_{15}Si_4$, leading a reversible Li/Si ratio of about 3.7. This reaction is accompanied by a rather flat plateau around 400 mV. The area encompassed by the equilibrium curves is attributed to hysteresis [8].

Obviously, the kinetics of Li-(de)intercalation is also essential from an application point of view. To characterize the charge transfer kinetics of the silicon/electrolyte interface, EIS was measured during the GITT measurements. The impedance spectra obtained during discharging $Li_{15}Si_4$ are presented in Fig. 7a, revealing two semi-circles, followed by a capacitor-like straight line. The width of the semi-circles observed at high frequencies is almost independent of the potential and can therefore be attributed to the SEI response. The second semi-circle on the other hand changes substantially as a function of the potential and can be attributed to the charge transfer reaction at the silicon/SEI interface. The EIS data were fitted with respect to the equivalent circuit presented in Fig. 7b. As the semi-circles were depressed, constant phase elements (CPEs) were adopted for both the SEI and charge transfer related capacitances. The equivalent circuit includes a series resistance (R_s), an SEI (R_{SEI} parallel to CPE_{SEI}), a charge transfer (R_{ct} and CPE_{dl}) and diffusion (Z_{diff}) elements.

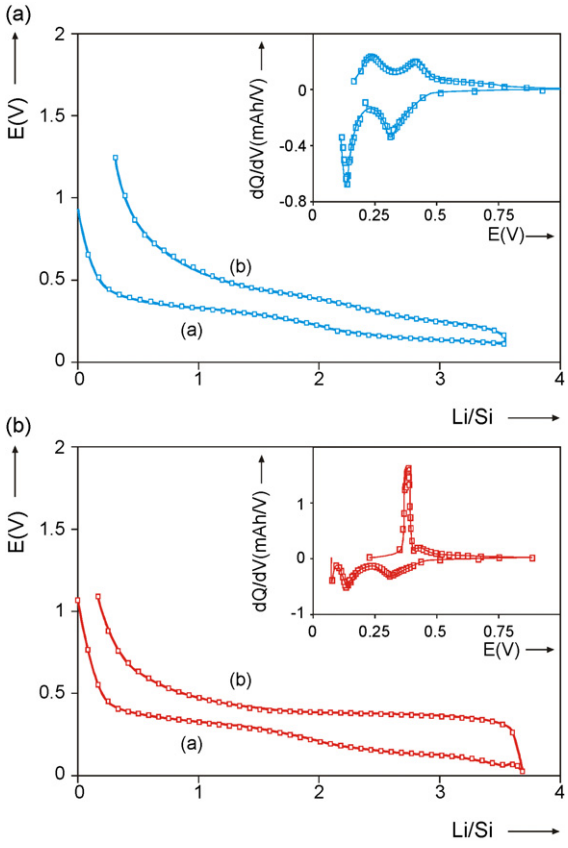

Fig. 6. Equilibrium curves of poly-Si obtained with Galvanostatic Intermittent Titration Technique (GITT). The cut-off potential values applied during charge are 50 and 0 mV, figures (a) and (b) respectively. The insets show the derivative of storage capacity with respect to potential. The charge is denoted on the curves as (a) and the discharge as (b) (Ref. [8]. Copyright Wiley-VCH Verlag GmbH & Co. KGaA. Reproduced with permission).

By equivalent circuit fitting, the resistance, capacitance and n values are obtained for different Li compositions. The corresponding results are plotted in Fig. 8. It can be concluded from Fig. 8a that the resistance associated with the SEI layer is almost constant. As the SEI can be considered as an ionic conductor and electronic insulator, it is not surprising to observe that its ionic resistance does not vary substantially. The reason for the variations observed at high Li compositions might result from a more complicated fit, as is also observed for the corresponding n values. Another reason for these variations might be that the SEI layer is changing its composition or thickness upon Li-deintercalation. Similar changes were already reported for other types of silicon thin-film electrodes [22].

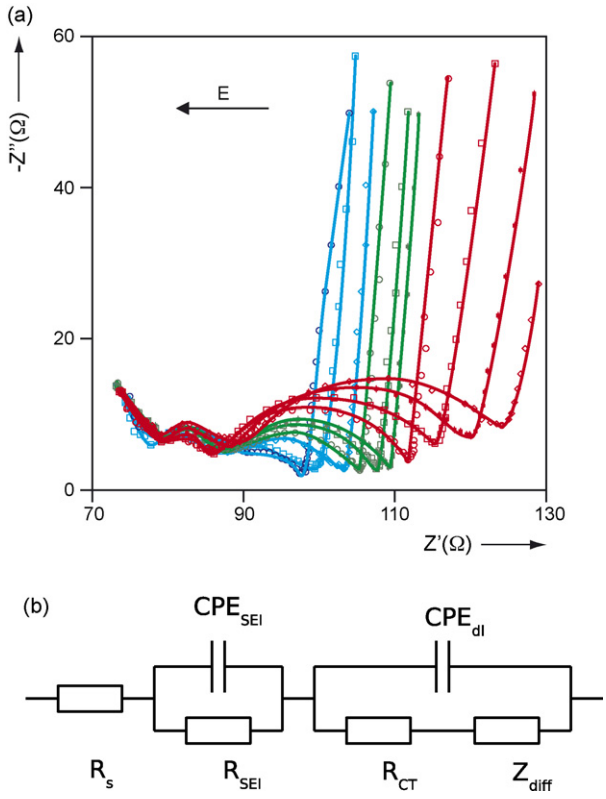

Fig. 7. (a) Impedance spectra measured during a GITT discharge of $Li_{15}Si_4$. (b) Equivalent circuit used to fit the EIS experimental data.

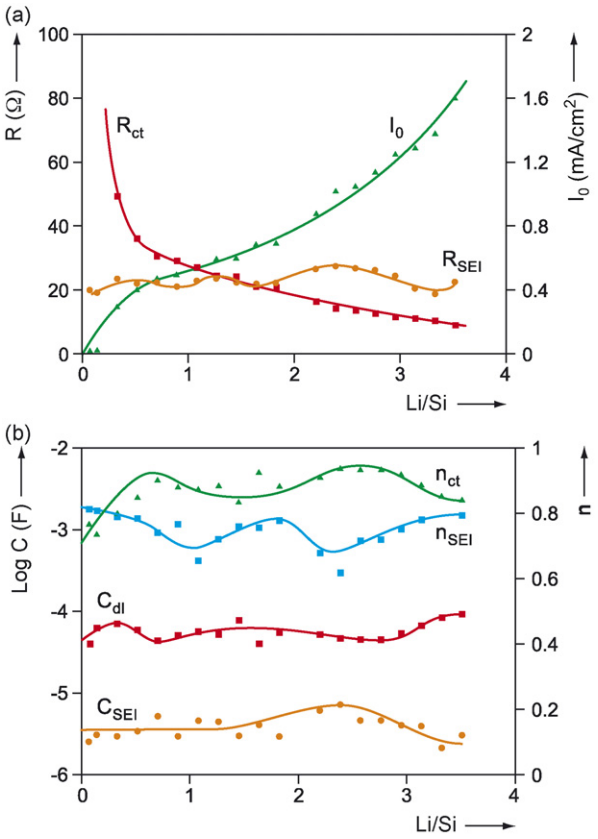

Fig. 8. Kinetics parameters extracted from EIS measurements performed during a GITT discharge of $Li_{15}Si_4$, as presented in Fig. 6b curve (b). The charge transfer and SEI resistances and exchange current density are presented in (a) while (b) presents the double layer and SEI capacitance and n values.

Fig. 8b shows the variation of the capacitance and n values. The capacitance associated with the SEI layer varies between 3 and 7 μF for an electrode having a footprint geometry of 1.77 cm^2 (Fig. 8b). Regarding the charge transfer, it is clear that the corresponding resistance decreases with increasing Li content (Fig. 8a). The double layer capacitance varies between 40 and 80 μF (Fig. 8b). The exchange current density (I_0), plotted in Fig. 8a, is derived from

$$I_0 = \frac{1}{A}\frac{RT}{nFR_{ct}} \quad (3)$$

in which A is the electrode area (cm^2), R is the gas constant (8.314 J mol^{-1} K^{-1}), T the absolute temperature, F the Faraday constant (96485 C mol^{-1}) and n is the number of transferred electrons during the rate determining step [23]. Arbitrarily, n is taken unity. As shown in Fig. 8a, high values of I_0 (low values of R_{ct}) are obtained, which implies that the rate at which electrons are transferred at the silicon/SEI interface is relatively fast.

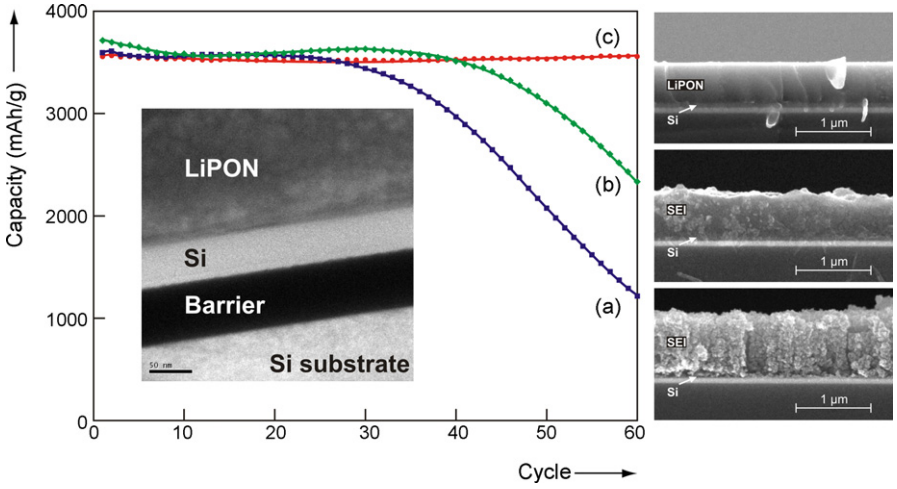

Fig. 9. Cycle-life of 50 nm thick poly-Si electrodes in conventional organic Li-ion battery electrolytes containing 1 M $LiPF_6$ in EC/DEC (a), 1 M $LiClO_4$ in PC (b) and of the same electrode covered with a LiPON solid-state electrolyte (c). Galvanostatic cycling was performed using a 1 C-rate current between 0 and 3 V *vs.* Li/Li^+. The inset picture shows an EFTEM photograph of the as-deposited LiPON-covered silicon electrode. The right hand side SEM cross-sections were taken after cycling in the different electrolytes.

Obviously, cycling is another key issue for rechargeable battery applications. The lifetime of 50 nm thick poly-Si anodes was investigated using two different liquid electrolytes, 1 M $LiClO_4$ dissolved in propylene carbonate and 1 M $LiPF_6$ dissolved in ethylene and diethyl carbonate, and amorphous lithium phosphorus oxynitride (LiPON) as solid-state electrolyte. Curves (a) and (b) of Fig. 9 show that cycling Si electrodes in conventional Li^+-salt containing organic electrolytes the storage capacity is stable up to about 30 or 40 cycles but starts to decline sharply afterwards. Strikingly, when in addition an inorganic solid electrolyte is used to cover the Si (as shown in the energy filtered TEM (EFTEM) inserted in Fig. 9) the capacity is maintained without observing any degradation (curve (c)). After cycling, the cycled Si electrodes were subjected to SEM. The existence of a SEI can beautifully be visualized by making use of Si wafers, easily facilitating to make cross-sections. SEM reveals that a thick and porous passivation layer (SEI) has been formed upon cycling in the case of the $LiPF_6$-based electrolyte (a) and $LiClO_4$-based electrolyte (b). The Si layer is hardly visible, as it seems to be "dissolved" within the SEI layer. Strikingly, when a LiPON layer covers Si, liquid electrolyte decomposition does not take place and the Si layer remains intact (c). Here, the SEI layer is completely absent and, consequently, the cycle life of the Si electrode is not negatively affected at all (Fig. 9, curve (c)).

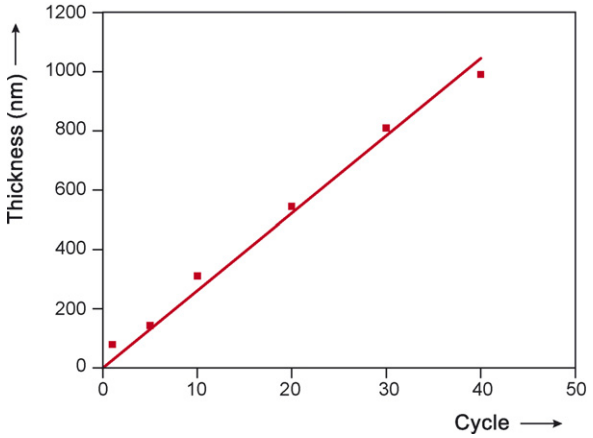

Fig. 11. Thickness of the SEI layer grown on top of poly-Si anodes in 1 M $LiPF_6$ in EC/DEC. The values were obtained from SEM cross-sections similar to that presented in Fig. 10c.

The impact of cycling on the SEI formation was quantified by investigating the samples with *ex situ* SEM at different stages of cycling. The evolution of the SEI morphology was studied as a function of cycle number in both liquid electrolytes on fully discharged

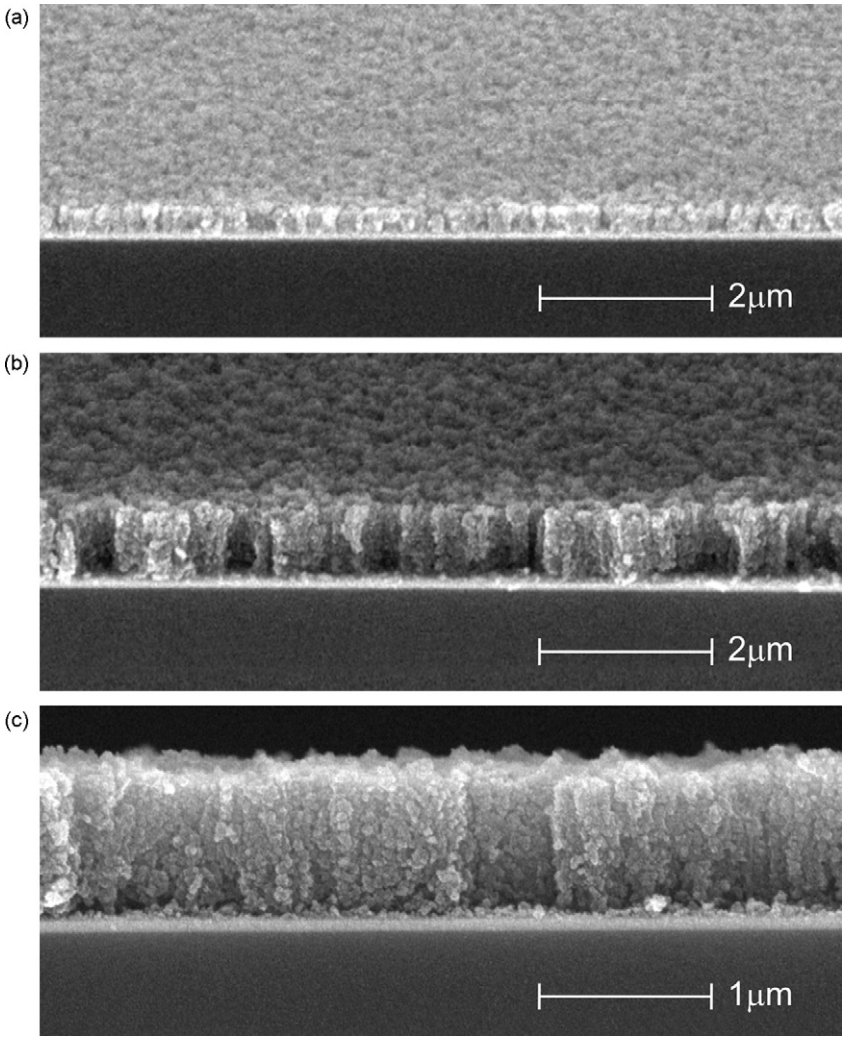

Fig. 10. SEM photographs of poly-Si samples deposited onto TiN, cycled at different stages with the same electrolyte (1 M $LiPF_6$ in EC/DEC). Pictures (a) and (b) were respectively taken with a tilting angle after 10 and 40 cycles and picture (c) is a cross-section view of picture (b).

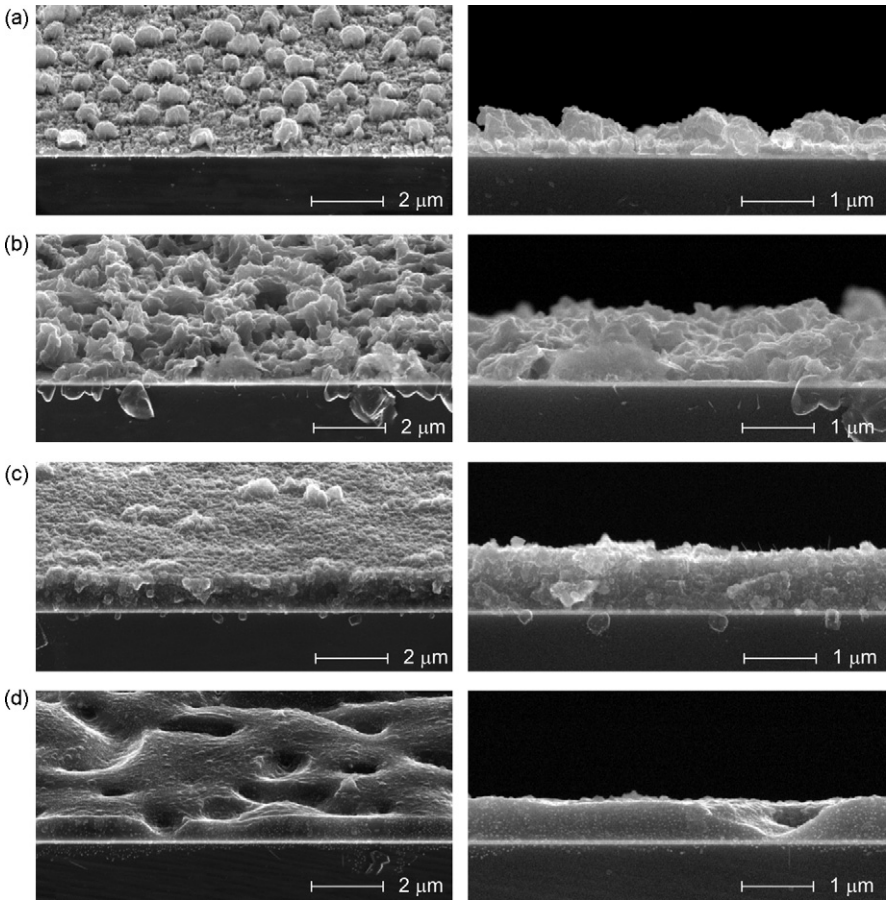

Fig. 12. SEM photographs of poly-Si samples deposited onto TiN, cycled in 1 M $LiClO_4$/PC. The left hand side pictures were taken with a tilting angle and the right hand side pictures are corresponding cross-sections. The samples were cycled 10 (a), 20 (b), 30 (c) and 40 (d) times.

electrodes. It was observed that the SEI layers formed on top of poly-Si anodes cycled in the $LiPF_6$-based electrolyte keep the same complex morphology upon growth. This is clearly presented in Fig. 10 for cycle number 10 and 40. A thick and very porous material, with a 'pillar-like' structure, has grown rather homogeneously on top of the anode material. A closer look with the SEM at the interface between the silicon and SEI layers did not clearly indicate the presence of the initial silicon film. This probably results from the fact that silicon becomes embedded, to some extent, within the SEI layer.

The growth of the SEI layer formed in the $LiPF_6$-based electrolyte is depicted in Fig. 11. The thickness of the film is plotted as a function of the cycle number. A clear linear relationship is observed, which indicates that the SEI is continuously formed during the (de)intercalation of silicon. A film of about 1 μm was found after 40 cycles. This is more than one order of magnitude thicker than the original Si electrode thickness.

In the case of Si anodes cycled in the $LiClO_4$-based electrolyte, it was found that the morphology of the SEI film formed on top of poly-Si anodes changed substantially upon cycling. Fig. 12 shows some SEM pictures taken at different cycle numbers. It seems that more cycling leads to a denser SEI layer. Indeed, the SEI layer observed after 10 cycles (Fig. 12a) reveals an 'island-like' morphology. After 20 cycles, the islands have grown and partly agglomerated (Fig. 12b). When cycled 30 times, the sample reveals a more or less continuous SEI film and the gaps between the islands visible in Fig. 12b are now filled (Fig. 12c). Finally, after 40 cycles (Fig. 12d), the film appears denser, smoother but showed more irregular suppressions, which may be due to the increasing stress within the layer. As already observed for the anode samples cycled in the $LiPF_6$-based electrolyte, the silicon anode layer is also not visible at the anode/SEI interface.

The observations made with these cycled silicon electrodes in the two liquid electrolytes indicate that the formation and the growth of an SEI layer are responsible for the capacity decay of the anodes. As known from literature, SEI films are usually composed of materials that are poorly electronically conductive [22]. Our SEM investigations show that silicon gets embedded within a complex SEI film. Consequently, the active silicon clusters slowly become electronically isolated, resulting in a loss of reversible capacity.

4. Conclusions

A new 3D-integrated all-solid-state battery concept has been proposed [4,8]. Starting from a high surface area silicon substrates obtained by micro-etching, this integrated battery concept is based on the step-conformal successive deposition of Li-diffusion barrier layers, high energy dense Si anodes, solid-state electrolytes, cathodes and current collectors. Owing to this unique surface area enhancement, the proposed battery concept will improve the storage capacities of future integrated all-solid-state Li-ion microbatteries significantly and offer interesting integration options.

A potential anode stack has been investigated. It comprises a substrate, a Li diffusion barrier layer and an anode material. Several Li diffusion barrier layer candidates were studied. Interesting Li diffusion barrier layers have been successfully identified. Sputtered and ALD TiN were shown to be promising candidates with respect to efficient Li-blocking. The reaction mechanism between

TiN and Li was investigated. Conversion or displacement reactions have been disregarded. Indeed, *ex situ* XRD did not show any change in crystallographic properties before and after cycling. Moreover, less than 0.02 Li was reversibly stored into TiN. Thus, the reaction mechanism between TiN and Li has still to be elucidated.

The thermodynamic and kinetic properties of LPCVD-grown poly-silicon electrodes have been studied with GITT and EIS. The impact of cycling on the SEI formation was quantified by investigating the samples with *ex situ* SEM at different stages of cycling. The corresponding results reveal that a thick SEI film grows upon cycling of Si anodes. Moreover, the silicon anode layer is not visible at the anode/SEI interface as if it was embedded within the complex SEI film. This can imply that the active silicon clusters slowly become electronically isolated and explain why a loss of reversible capacity is observed.

Acknowledgements

We gratefully thank Jeroen van Zijl, Jan Verhoeven, Harold Roosen, Tiny den Dekker and Loc Quang Huynh for the preparation of the various sputtered and LPCVD layers. The authors are also indebted to Monique Vervest, Hetty de Barse, Monja Kaiser, Thuy Dao, Peer Zalm and Peter Graat for the material characterizations. A special thank is given to Harm Knoops and Erwin Kessels for providing TiN samples grown by ALD. Finally, the authors would like to acknowledge Frans Schraven for his visual works. This research has been financially supported by the Dutch Foundation *SenterNovem*.

References

[1] E. Aarts, R. Collier, E. van Loenen, in: B. de Ruyter (Ed.), Ambient Intelligence, Springer-Verlag, New York, 2003.
[2] A. Toffler, in: A. Toffler (Ed.), Future Shock, Bantam Books, New York, 1970.
[3] W. Verhaegh, E.H.L. Aarts, J. Korst, in: W. Verhaegh, E.H.L. Aarts, J. Korst (Eds.), Algorithms in Ambient Intelligence, Kluwer Academic Publishers, Dordrecht, 2003.
[4] P.H.L. Notten, F. Roozeboom, R.A.H. Niessen, L. Baggetto, Adv. Mater. 19 (2007) 4564–4567.
[5] J.B. Bates, N.J. Dudney, D.C. Lubben, G.R. Gruzalski, B.S. Kwak, X. Yu, R.A. Zuhr, J. Power Sources 54 (1995) 58–62.
[6] J.W. Long, B. Dunn, D.R. Rolison, H.S. White, Chem. Rev. 104 (2004) 4463–4492.
[7] D. Golodnitsky, M. Nathan, V. Yufit, E. Strauss, K. Freedman, L. Burstein, A. Gladkich, E. Peled, Solid State Ionics 177 (2006) 2811–2819.
[8] L. Baggetto, R.A.H. Niessen, F. Roozeboom, P.H.L. Notten, Adv. Funct. Mater. 18 (2008) 1057–1066.
[9] M. Armand, J.-M. Tarascon, Nature 451 (2008) 652–657.
[10] F. Roozeboom, R. Elfrink, T.G.S.M. Rijks, J. Verhoeven, A. Kemmeren, J. van den Meerakker, Int. J. Microcircuits Electron. Packag. 24 (2001) 182–196.
[11] N. Pereira, M. Balasubramanian, L. Dupont, J. McBreen, L.C. Klein, G.G. Amatucci, J. Electrochem. Soc. 150 (2003) A1118–A1128.
[12] N. Pereira, L. Dupont, J.-M. Tarascon, L.C. Klein, G.G. Amatucci, J. Electrochem. Soc. 150 (2003) A1273–A1280.
[13] S.P. Garg, M. Venkatraman, N. Krishnamurthy, J. Alloy Ph. Diagr. 6 (1990) 8–9.
[14] J. Weeks, Trans. ASM 58 (1965) 302.
[15] H.C.M. Knoops, L. Baggetto, E. Langereis, M.C.M. van de Sanden, J.H. Klootwijk, F. Roozeboom, R.A.H. Niessen, P.H.L. Notten, W.M.M. Kessels, ECS Trans. 11 (2007) 45–54.
[16] H.C.M. Knoops, L. Baggetto, E. Langereis, M.C.M. van de Sanden, J.H. Klootwijk, F. Roozeboom, R.A.H. Niessen, P.H.L. Notten, W.M.M. Kessels, J. Electrochem. Soc. (2008), in press.
[17] S.-J. Lee, J.-K. Lee, S.-H. Chung, H.-Y. Lee, S.-M. Lee, H.-K. Baik, J. Power Sources 97/98 (2001) 191–193.
[18] G. Raghavan, C. Chiang, P.B. Anders, S.-M. Tzeng, R. Villasol, G. Bai, M. Bohr, D.B. Fraser, Thin Solid Films 262 (1995) 168–176.
[19] S.B.S. Heil, E. Langereis, A. Kemmeren, F. Roozeboom, M.C.M. van de Sanden, W.M.M. Kessels, J. Vac. Sci. Technol. A23 (4) (2005) L5–L8.
[20] T.D. Hatchard, J.R. Dahn, J. Electrochem. Soc. 151 (2004) A838–A842.
[21] C. van der Marel, G.J.B. Vinke, W. van der Lugt, Solid State Commun. 54 (1985) 917–919.
[22] Y.-M. Lee, J.Y. Lee, H.-T. Shim, J.K. Lee, J.-K. Park, J. Electrochem. Soc. 154 (2007) A515–A519.
[23] A.J. Bard, L.R. Faulkner, in: D. Harris, E. Swain, C. Robey, E. Aiello (Eds.), Electrochemical methods; fundamentals and applications, second edition, John Wiley & Sons, New York, 2001.